Check for updates

Near-infrared broadband cavity-enhanced sensor system for methane detection using a wavelet-denoising assisted Fourier-transform spectrometer

Kaiyuan Zheng,[a,2] Chuantao Zheng, [iD] *[a] Zidi Liu,[a] Qixin He,[a] Qiaoling Du,[a] Yu Zhang, [iD] [a] Yiding Wang[a] and Frank K. Tittel[b]

The majority of broadband cavity-enhanced systems are used to detect trace gas species in the visible spectral range. We demonstrated a broadband cavity-enhanced sensor system in combination with a Fourier-transform spectrometer (FTS) in the near-infrared (near-IR) region for methane (CH_4) detection. Light from a tungsten–halogen lamp was coupled into a high-finesse cavity and the light leaking from the cavity was imaged onto the FTS. An optimal incident beam diameter of 2.25 cm was required in the condition of a 40 cm-long cavity of a 2.5 cm diameter and a 100 cm radius of curvature (RoC) mirror. The CH_4 sensor system was capable of operating at a temperature of 300 K and 1 atm gas pressure. Based on an Allan variance analysis, a minimum detectable absorption coefficient of 4.6×10^{-7} cm^{-1} was achieved. A wavelet denoising (WD) method was introduced in the retrieval of the gas concentration, which improved the measurement precision from 10.2 parts-per-million in volume (ppmv) to 5.3 ppmv with an enhancement factor of 2 for a 20 min averaging time. The near-IR broadband cavity-enhanced sensor system can also be used to measure high-resolution absorption spectra of other atmospheric trace gas species.

1. Introduction

Gas detection and precise concentration measurements are keys to many fields ranging from industrial process control to atmospheric pollution monitoring.[1,2] Different spectroscopic approaches, especially broadband absorption spectroscopy for exploiting multiplexing features in a wide spectral range have been reported such as broadband cavity ring-down spectroscopy (CRDS),[3–7] broadband cavity-enhanced absorption spectroscopy (CEAS) using pulsed lasers,[8–10] and the incoherent broadband cavity-enhanced absorption spectroscopy (IBBCEAS).[11] These techniques offer different advantages and disadvantages in terms of selectivity, portability, sensitivity and cost.

Among these techniques for broadband spectral absorption measurements, the IBBCEAS method is theoretically straight forward and capable of high sensitivity and high spatial resolution. Due to the great potential for trace gas detection, the IBBCEAS technique has been significantly developed.[12–16]

Nevertheless high resolution absorption measurements in the near-IR spectral region are experimentally challenging because of weak transitions and disturbances from vibrational overtones and combination of basic patterns.[17] However, the application of IBBCEAS technique in conjunction with a high-resolution Fourier-transform spectrometer (FT-IBBCEAS) achieves a relatively high selectivity and sensitivity, especially in the near-IR region. Several sensor systems based on FT-IBBCEAS were reported.[18–22] The commonly used light sources in FT-IBBCEAS are supercontinuous (SC) sources owing to their high spatial coherence and high brightness. In 2011, Denzer *et al.* proposed a FT-IBBCEAS system using SC source and a 25 cm-long cavity formed by two highly-reflective mirrors (99.98%).[19] A minimum detectable absorption coefficient of 4×10^{-9} cm^{-1} was obtained with a 4 min averaging time. In 2015, Chandran *et al.* reported a SC-based FT-IBBCEAS set-up to record the absorption of 1,4-dioxane with a resolution of 0.08 cm^{-1}. The cavity has a length of 644 cm consisting of two highly-reflective mirrors (99.9%), leading to a detection limit of 8×10^{-8} cm^{-1} in a 120 min averaging time.[21]

Despite the higher brightness and better spatial coherence of the SC source, the signal to noise ratio (SNR) is not much higher when compared to a Xe lamp.[23] Moreover, a SC source is not easy to operate and is costly so far. Hence a low cost and

[a]*State Key Laboratory of Integrated Optoelectronics, College of Electronic Science and Engineering, Jilin University, 2699 Qianjin Street, Changchun 130012, China. E-mail: zhengchuantao@jlu.edu.cn; Tel: +86-13756090979*

[b]*Department of Electrical and Computer Engineering, Rice University, 6100 Main Street, Houston, TX 77005, USA*

high power, Xe lamp was used as an alternate light source in FT-IBBCEAS. This type of light source produces a continuum white light that covers the spectral region from UV to near-IR. A Xe lamp also provides a high luminous output as well as insensitivity to intensity fluctuations. Several Xe lamp-based FT-IBBCEAS set-ups were reported to confirm the proof-of-principle of this technique by measuring weak atmospheric transitions of different gas species. In 2007, a FT-IBBCEAS set-up based on a Xe lamp was employed to measure the spin-forbidden B-band of gaseous oxygen (O_2) and several weak absorption transitions of water vapor (H_2O) in the visible region.[24] In 2008, the overtone bands of CO_2, OCS, and $HD^{18}O$ were measured in the near-IR region using FT-IBBCEAS.[23]

The wavelet denoising (WD) method introduced in the early 1990s is a mathematical transformation for decomposing functions.[25] Due to its ability of suppressing noise in both time- and frequency-domain for the enhancement of SNR, WD has been successfully employed in image and signal processing in recent years.[26,27]

In this work, due to a better stabilization of the output intensity in the near-IR region, a high-power tungsten–halogen lamp was employed instead of a Xe lamp. A simulation of the optimal incident beam diameter was carried out using MATLAB. The consequences of cavity length, mirror diameter and RoC of the mirror on the optimal incident beam diameter were analyzed. Furthermore, a simulation of the light beam propagation inside the cavity is performed by using the optimized parameters. WD is also adopted in the sensor system for data processing in order to improve the accuracy and sensitivity of the reported sensor system.

2. Theory

2.1 Cavity modeling and analysis

A generic model of the light beam propagation inside the cavity is shown in Fig. 1. The incident broadband light beam is simplified to a single ray (the red lines in Fig. 1) and thus an optical matrix theory can be used for a beam propagation analysis. The light ray from the light source is firstly coupled to M_1 parallel to the optical axis with a specific distance from the axis, and then the ray is reflected back and forth between M_1 and M_2. If the distance between the incident ray and the

optical axis increases to a certain value, light will exit the cavity after multiple reflections. The transfer matrix for one round trip can be expressed as:

$$T = \begin{bmatrix} 1 & 0 \\ -\frac{2}{RoC} & 1 \end{bmatrix} \begin{bmatrix} 1 & L \\ 0 & 1 \end{bmatrix} \begin{bmatrix} 1 & 0 \\ -\frac{2}{RoC} & 1 \end{bmatrix} \begin{bmatrix} 1 & L \\ 0 & 1 \end{bmatrix} = \begin{bmatrix} E & F \\ G & H \end{bmatrix} \quad (1)$$

After n round trips in the cavity, the total optical propagation matrix is written as

$$T^n = \begin{bmatrix} E_n & F_n \\ G_n & H_n \end{bmatrix}$$
$$= \frac{1}{\sin \varphi} \begin{bmatrix} E \sin n\varphi - \sin(n-1)\varphi & F \sin n\varphi \\ G \sin n\varphi & H \sin n\varphi - \sin(n-1)\varphi \end{bmatrix} \quad (2)$$

$$\varphi = \arccos\left(\frac{E+H}{2}\right) \quad (3)$$

In IBBCEAS, the effective optical path length is expressed as $L_{eff} = L/(1-R)$, here R is the reflectivity of the mirror. In this model, the effective optical path length is $2kL$. And k represents the number of reflections. Therefore, we can deduce that $L/(1-R) = 2kL$ and $k = 1/(2(1-R))$. In our sensor system, the maximum value of R is 0.9994 and thus k is determined to be 830.

If all the light rays are reflected in the cavity without leakage, the high-finesse cavity is considered as a stable cavity. The stability condition is expressed as $-1 < (E+H)/2 < 1$. When the light rays are reflected 830 times in the cavity, there is a maximum value of D satisfying the stability condition, which is defined as the optimal incident light beam diameter. A beam diameter that is smaller than the maximum value can not only ensure the stability of the cavity, but also improves the robustness of the sensor system.

2.2 Simulation and optimization

In general, the maximum value of D (defined as D_{max}) for obtaining a stable cavity is a function (defined as f) of D, L, d and RoC, expressed as

$$D_{max} = f(D, L, d, RoC)|_{parallel} \quad (4)$$

where f is not an explicit function but can be achieved by using MATLAB simulation based on the transmission matrix of the cavity propagation. D_{max} can be determined by the following condition

$$\begin{cases} D \leq D_{max}, \text{cavity is stable} \\ D > D_{max}, \text{cavity is unstable} \end{cases} \quad (5)$$

Table 1 shows the range of different significant parameters and their optimized values. The ranges were 0–200 cm for L, 0–2.5 cm for d, 0–400 cm for RoC. The relationship between D and these parameters is presented in Fig. 2.

Assuming that M_1 and M_2 have the same diameter (d) of 2.5 cm and the RoC is selected to be 50, 100, 150 and 200 cm, respectively, the relationship between D and L is represented in Fig. 2(a). When $L = RoC/2$ (semi-confocal cavity), D becomes
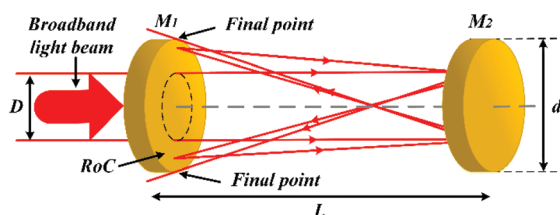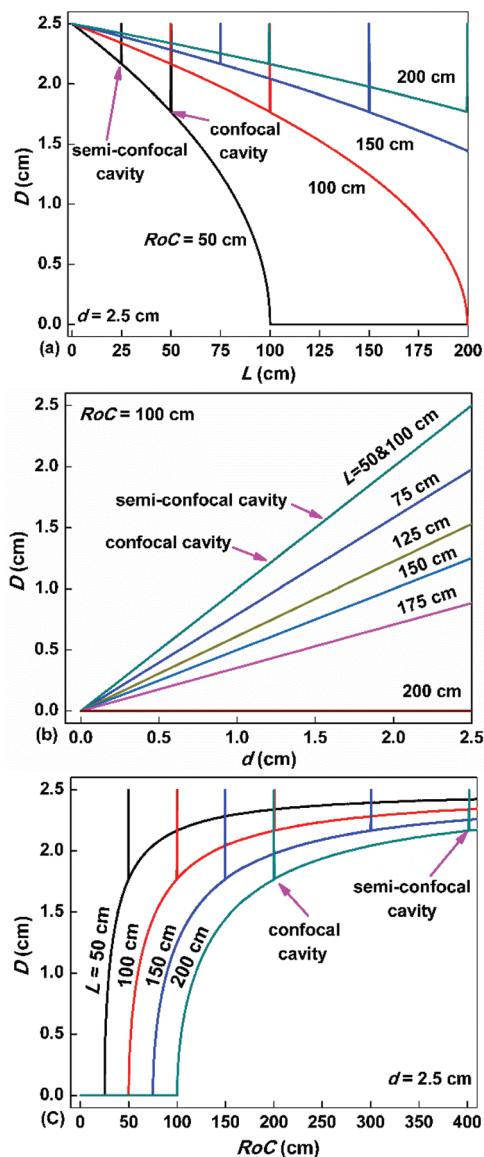

Fig. 1 Modeling of the light beam propagation inside the cavity (red lines). M_1 and M_2 are two plano-concave mirrors with high reflectivity, D is the diameter of broadband light beam, L is the cavity length, d is the diameter of the mirror and RoC is the radius of curvature of the mirror.
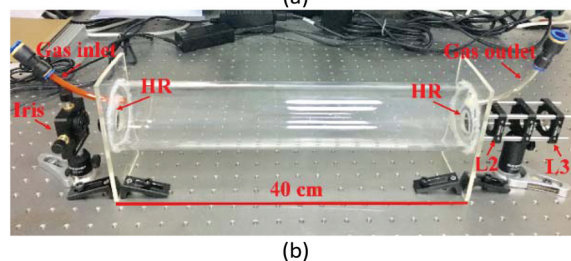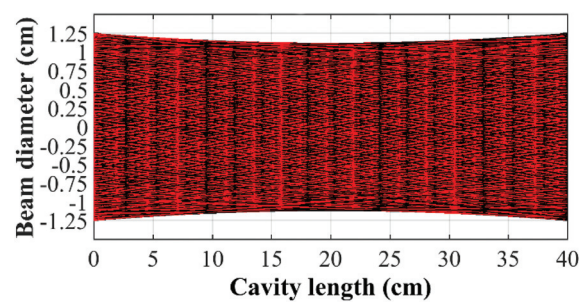
Table 1 The ranges of L, d, RoC, D and their optimized values

Parameter	D (cm)	L (cm)	d (cm)	RoC (cm)
Range	0–2.5	0–200	0–2.5	0–400
Optimized value	2.25	40	2.5	100

Fig. 2 (a) Relationship between D and L, where d = 2.5 cm, RoC = 50, 100, 150, 200 cm. (b) Relationship between D and d, where RoC = 100 cm, L = 50, 75, 100, 125, 150, 175, 200 cm. (c) Relationship between D and RoC, where d = 2.5 cm, L = 50, 100, 150, 200 cm.

Fig. 3 (a) Simulated light beam propagation between two cavity mirrors with optimized parameters. (b) Photograph of the fabricated cavity with a length of 40 cm and a volume of 1 L.

Suppose that the RoC of the mirror is 100 cm and L varies from 50 to 200 cm. The relationship between D and d is demonstrated in Fig. 2(b). Under the condition of the same L, D rises gradually with an increase of d. For the same d, the value of D of the semi-confocal cavity and that of the confocal cavity are the largest and the same, which can be found by the overlaping curves of L = 50 cm and L = 100 cm in Fig. 2(b). After removing these two points, D decreases with increasing L.

If d is 2.5 cm and L is selected to be 50, 100, 150 and 200 cm, respectively, the relationship between D and RoC is shown in Fig. 2(c). For the condition of a fixed L, D increases slightly if RoC increases from 0 to L/2. However, when RoC increases from L/2 to L, D increases sharply and reaches its maximum value (i.e. d) in the confocal configuration. D increases slowly and tends to be stable until RoC equals $2L$ in a semi-confocal configuration.

As the result of optimization for a cavity with a length of 40 cm, a mirror diameter of 2.5 cm and a RoC of 100 cm, an optimal incident beam diameter of 2.25 cm is obtained. A simulation of the light beam propagation in the cavity by using the optimized parameters is demonstrated in Fig. 3(a). All rays are found to be limited to the cavity, resulting in a stable cavity. A photograph of the fabricated cavity with a volume of 1 L is shown in Fig. 3(b). An iris placed in front of the first mirror is used to limit the incident light beam diameter to 2.25 cm as required.

3. Experimental set-up

The FT-IBBCEAS experimental set-up is illustrated in Fig. 4. The broadband light from a tungsten halogen lamp (LSH-T150, 150 W) was collected by a spherical metallic mirror
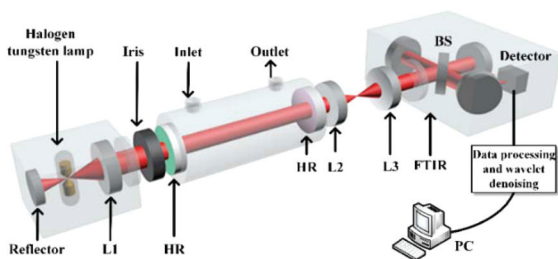
the largest and is equals to d. The same result is found when L = RoC (confocal cavity). Excluding these two points, D decreases with increasing L. Furthermore, when L changes from RoC/2 to RoC, the decay rate of D is obviously faster than that of L from 0 to RoC/2, which indicates that the latter cavity is more stable.

Fig. 4 Schematic of the experimental set-up. L1 is a plano-convex lens used to collimate the light from the tungsten−halogen lamp. HR is a highly-reflective mirror used to form an optical cavity and a gas cell. L2 and L3 are achromatic lenses used to focus and collimate the light leaking through the cavity. FTIR is a Fourier-transform infrared spectrometer. BS is a beam splitter. A PC is used for data processing and wavelet denoising.

and then coupled into a 40 cm-long optical stable cavity by means of a plano-convex lens. According to the optimization results above, an iris was used in front of the cavity to adjust the incident beam diameter to 2.25 cm, leading to a stable optical cavity with a sufficiently high SNR. The optical cavity consisted of two plano-concave mirrors (Layertec GmbH, 2.5 cm diameter, Germany) with a RoC of 1 m and a volume of 1 L. Two lenses were used to focus the cavity output beam and to collimate the radiation into a circular entrance aperture of a commercial high-resolution FTIR spectrometer (Thermo Fisher Scientific, model Nicolet iS50 FTIR, USA). The light was imaged onto a DLaTGS detector and the obtained signal was processed by a pre-amplifier with a gain of 8. The output signal from the pre-amplifier was processed by an analog-to-digital converter (ADC) followed by WD processing. Then the obtained signal was Fourier transformed on a PC using OMNIC software (Thermo Fisher Scientific, USA). The FTIR spectrometer exhibits a major advantage, which is much easier for optical alignment without the need for phase-sensitive detection. The resolution of the CH_4 spectrum was 0.5 cm^{-1}. The spectrum was obtained by the acquired averaging of 256 interferometer scans, leading to an acquisition time of 20 min. A visible He–Ne laser (not shown in Fig. 4) was used for alignment of the optical path to maximize the total transmission of the cavity. Furthermore, nitrogen (N_2) was used as a balance gas to mix with CH_4 in order to obtain gas samples with different concentration levels *via* a gas mixing system (Series 4000, Environics, USA).

4.   Results and discussion

4.1 CH_4 absorption in the near-IR region

Under the experimental condition of 1 atm pressure and 300 K temperature, the CH_4 absorption spectrum in the near-IR spectral region of 5930–6150 cm^{-1} is shown in Fig. 5(a). The simulation from the high resolution transmission (HITRAN) database also illustrates the inter-comparison of the absorption characteristics of potential interferences from CO_2 and H_2O at
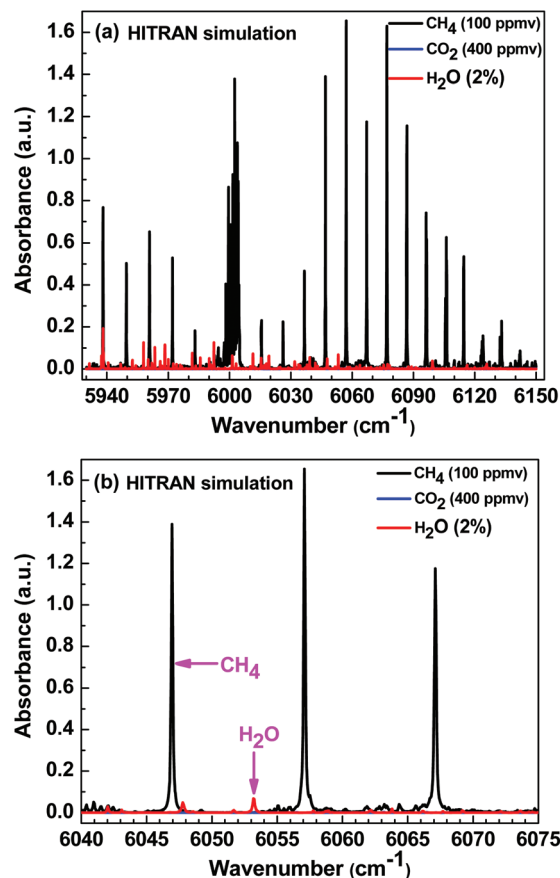

Fig. 5 (a) HITRAN simulation of the absorption spectra of CH_4 (100 ppmv) at 5930–6150 cm^{-1}, along with two major abundant molecular species of CO_2 (400 ppmv) and H_2O (2%), at experimental conditions of 1 atm pressure and 300 K temperature. (b) HITRAN simulation of the absorption spectra of CH_4 (100 ppmv) at 6040–6075 cm^{-1} demonstrating the interference-free spectral line at the same experimental conditions.

~1.65 μm. Furthermore, in order to check the potential interference of H_2O (2%) and CO_2 (400 ppmv) in the region of 6040–6075 cm^{-1}, a simulation was implemented and is shown in Fig. 5(b). It was found that the overtone bands of CH_4 are free from the interferences of H_2O and CO_2, which ensures the detection selectivity of CH_4.

4.2   Mirror reflectivity calibration

In order to determine the absorption coefficient of the target gas species, it is necessary to calibrate the wavelength-dependent reflectivity of the cavity mirrors. In this experiment, the mirror reflectivity was determined by comparing the single pass spectrum (*i.e.* non-cavity enhanced) with those of the cavity-enhanced spectra.[18] A CH_4 gas sample with a concentration level of 1000 ppmv was used for analysis. The single pass spectrum is carried out while the cavity-enhanced absorption spectrum is analyzed by eqn (6)

$$\frac{I_0}{I} - 1 = \frac{\alpha L}{1 - R} \qquad (6)$$

where α is the absorption coefficient, and I and I_0 are the measured spectral signals when the cavity is filled with the target gas and pure N_2, respectively. The experimentally determined mirror reflectivity associated with the effective optical path length is displayed in Fig. 6. The maximum mirror reflectivity was determined to be 99.94%, resulting in an effective optical length of 667 m, and thus an enhancement factor of 1666 was obtained in comparison to the single pass. Moreover, a significant enhancement of path length was observed from 6000 to 6100 cm^{-1}, which is located in the Q-branch and R-branch of the $2v_3$ overtone band of the CH_4 absorption spectrum.

4.3 CH_4 sensing performance

In IBBCEAS, the absorption coefficient α for the trace gas species inside the cavity is expressed as[15]

$$\alpha = \left(\frac{I_0}{I} - 1\right)\left(\frac{1-R}{L}\right) = \sum_i n_i \cdot \sigma_i(s_i + t_i\lambda) + p\lambda + q \quad (7)$$

where n_i (molecule per cm^3) represents the fit coefficient (*i.e.* the number density); σ_i (cm^2 per molecule) is the reference cross section of the i_{th} absorber which is convoluted with the instrument function; s_i and t_i are the shift and squeeze values of the reference spectrum to correct the wavelength calibration, respectively; $p\lambda + q$ accounts for the background effects resulting from lamp emission fluctuations and system drift. In data fitting, the CH_4 absorption line parameter was obtained from the HITRAN database and the Voigt broadening of the CH_4 lines at 296 K and at 1 atm were taken into consideration.

In order to evaluate the sensor performance with the FT-IBBCEAS instrument, the absorption spectrum of CH_4 of the $2v_3$ overtone transitions was measured in the spectral region between 5930 and 6150 cm^{-1}. High-resolution absorption spectra of the cavity filled with CH_4 (1000 ppmv) at an atmospheric pressure is shown in Fig. 7(a). The spectral resolution of the CH_4 spectrum was set to 0.5 cm^{-1}. The spectrum was averaged by 256 times in an averaging time of 20 minutes.
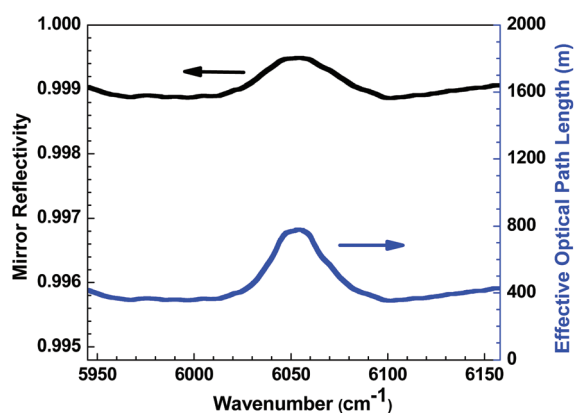

Fig. 6 Curves of the mirror reflectivity and the effective optical path length of the cavity *versus* wavenumber.
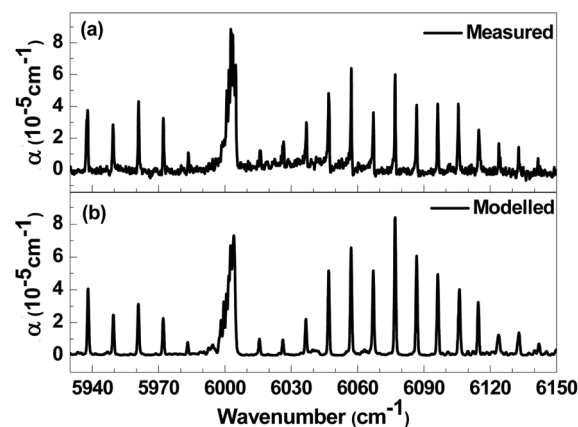

Fig. 7 (a) P, Q, R-branch of the $2v_3$ overtone of CH_4 measured in ambient air at atmospheric pressure using the FT-IBBCEAS. Measurement time: 20 min; resolution: 0.5 cm^{-1}. (b) Modelled least-square fit spectrum in the same region using the HITRAN database.

The fitted spectrum using the HITRAN database is shown in Fig. 7(b), which was in excellent agreement with the measured spectrum. The Q-band and several R-bands of the CH_4 spectrum appear to be stronger than the modelled one, which is due to the increased effective optical path length due to higher reflectivity in this spectral region.

In order to estimate the sensor performance, a fitting window of 6040–6075 cm^{-1} with a large effective optical path length was selected. The dependence of the fitting parameters on the spectral range in retrieving concentration was assessed for several wavenumber windows between 6040 and 6075 cm^{-1}. Depending on the width of the spectrum range, the retrieved number densities of CH_4 molecules varied between 6.368×10^{15} and 6.377×10^{15} molecule per cm^3 with an error of <0.6%. These results indicate that it is not critical to select a specific spectral range for fitting. In this experiment, the fitting range is selected from 6040 to 6075 cm^{-1}, which include the three strongest CH_4 absorption lines.

The experimental set-up was then applied to determine the sensor response by repeating a CH_4 measurement at different concentration levels. The commercial gas mixing system was used to generate a series of gas samples with different concentration levels and then supplied to the sensor system. Three strong absorption peaks in the fitting range of 6040–6075 cm^{-1} were selected for a concentration determination. The measured absorption spectra of the CH_4 samples with different mixing ratios are depicted in Fig. 8(a). The absorption coefficient rises as the concentration increases. The relationship between the maximum absorption coefficient at the three absorption peaks (6046.95 cm^{-1}, 6057.09 cm^{-1}, 6067.10 cm^{-1}, noted as peak1, peak2 and peak3) and the CH_4 concentration levels is depicted in Fig. 8(b), (c) and (d). All of the trends prove linear relationships between the absorption coefficient and the CH_4 concentration level.

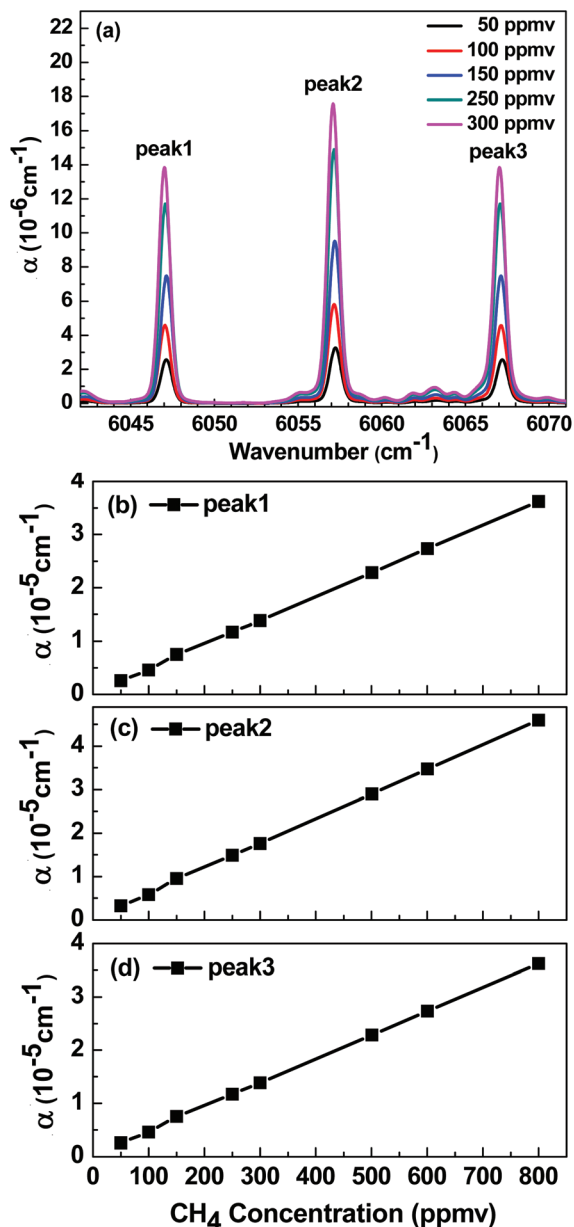A correlation plot of different CH_4 concentration levels measured by FT-IBBCEAS *versus* nominal concentrations is

Fig. 8 (a) Measured absorption spectra of CH₄ with different concentration levels in the fitting range. Relationships between the maximum absorption coefficient of (b) peak1, (c) peak2, (d) peak3 and different CH₄ concentration levels, respectively.

Fig. 9 Correlation plot of the CH₄ concentration measured by the sensor system and the nominal concentration generated by the standard gas mixing system.

Fig. 10 (a) Time series of the measurement results of the CH₄ sample with zero concentration. (b) Allan variance analysis of the FT-IBBCEAS CH₄ sensor system.

shown in Fig. 9. The nominal concentration is generated by the standard gas mixing system, and the measured concentration is obtained by the FT-IBBCEAS sensor system. The correlation plot indicates a good linear relationship ($R^2 = 0.99949$) between the two groups of concentration values. These results validate the accuracy of the FT-IBBCEAS instrument with a highly-linear response to the nominal concentration, which proves the feasibility of this method for the application in trace gas sensing.

An Allan variance analysis was used to evaluate the stability and sensitivity of the FT-IBBCEAS sensor system, which illus-
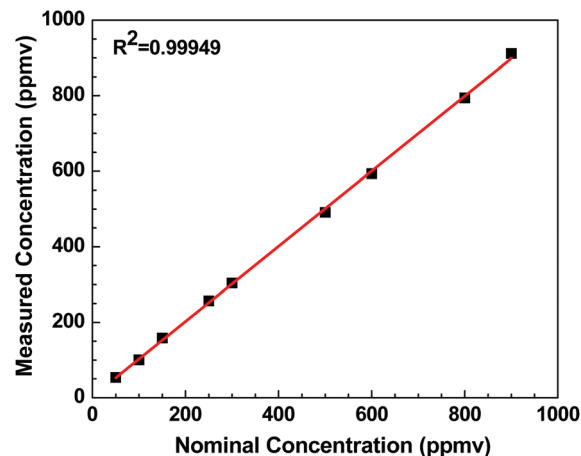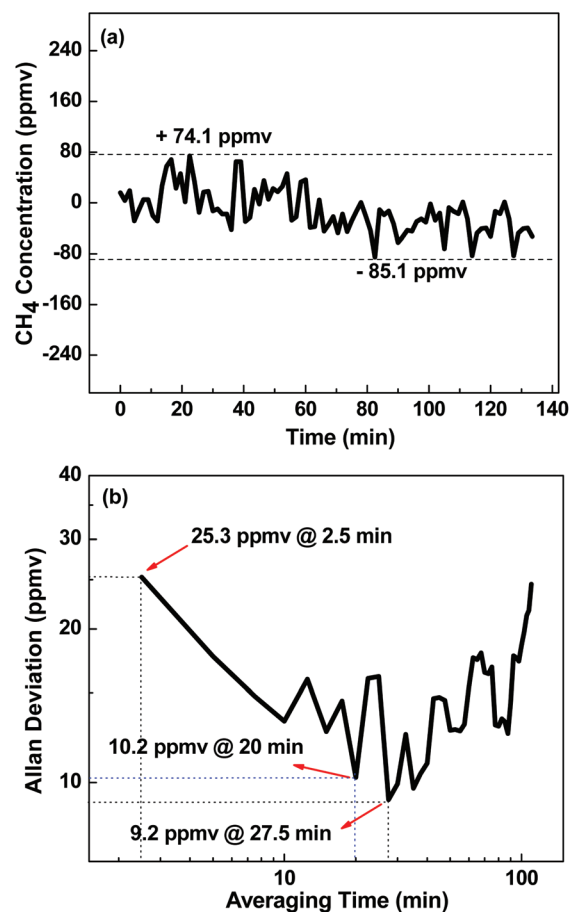
trated the noise characteristics of the system and provided the optimal averaging time for achieving the best stability. Fig. 10(a) shows ~2 h time series measurement results in a

pure N_2 atmosphere at a flow rate of 300 sccm. The Allan variance analysis result is shown in Fig. 10(b). The Allan variance decreases with the averaging time in the White-Gaussian noise dominated region. As the averaging time is longer than 27.5 min, the noise increased due to the system drift. Therefore, measurements should be done prior to this time to avoid the system drift. At a 2.5 min averaging time (32 averaged spectra), the detection limit (1σ) is 25.3 ppmv. The measurement precision can be further improved to 9.2 ppmv with an averaging time of 27.5 min (352 averaged spectra). In addition, for a 20 min averaging time (256 averaged spectra) used in this experiment, a detection limit of 10.2 ppmv is achieved, which

represents a compromise between sensitivity and long acquisition time.

4.4 Application of WD to CH_4 concentration retrieval

The WD technique can effectively suppress the noise in both time- and frequency-domains. To further improve the precision and sensitivity of this sensor system, a WD method was applied for the retrieval of CH_4 concentration level. For a signal $f(t)$ in the time-domain, the wavelet transformation is described as

$$Wf(m,n) = \frac{1}{\sqrt{m}} \int_{-\infty}^{+\infty} f(t)\psi^* \left(\frac{t-n}{m}\right) \mathrm{d}t \qquad (8)$$

where ψ is a wavelet function, m is the scale factor and n is the transition factor. WT is performed by moving a small wavelet function scaled with m and expressing the fit at every position in the coefficient $Wf(m,n)$.[28,29] The WD method includes three key parts, *i.e.* the wavelet basis function, the wavelet decomposition level and the wavelet threshold with its threshold function.[30] For an optimal combination of these factors, 'sym8' was chosen as the optimal wavelet basis function, a fifth level was considered to be the optimal decomposition level, and a threshold with the local threshold function were used to suppress the noise in the retrieval.

An experimental absorption spectrum of CH_4 measured by FT-IBBCEAS associated with its fitting curve is shown in Fig. 11. Without WD, the standard deviation of the fitting residual (1σ) is 8.5×10^{-7} cm^{-1}. With WD, the standard deviation is reduced to 4.6×10^{-7} cm^{-1}. The SNR of the CH_4 absorption spectrum can be estimated from the ratio of the maximal absorption difference to the standard deviation of the residual spectrum.[31] A SNR of 6.8 is deduced from the raw absorption spectrum, leading to a detection limit (1σ) of 10.2 ppmv for the FT-IBBCEAS instrument. With WD, the detection limit was decreased to 5.3 ppmv, indicating an improvement by a factor of 2 in the detection precision. The results indicate that the WD is an efficient denoising tool in enhancing the sensitivity and precision of trace gas sensing.

5. Conclusions

A tungsten–halogen lamp based FT-IBBCEAS sensor system was demonstrated for CH_4 detection in the near-IR region. Cavity modeling and analysis were performed, and the incident beam diameter was optimized for achieving a stable cavity. CH_4 measurements were conducted to evaluate the sensor performance. A detection limit (1σ) of 25.3 ppmv was achieved for a 2.5 min averaging time, which could be further improved to 9.2 ppmv with an averaging time of 27.5 min. The WD method was used for concentration retrieval of FT-IBBCEAS for performance improvement. The CH_4 measurement precision was improved to 5.3 ppmv with an enhancement factor of 2 in an averaging time of 20 min by the use of WD, indicating the potential application of the widely used FT-IBBCEAS technique.
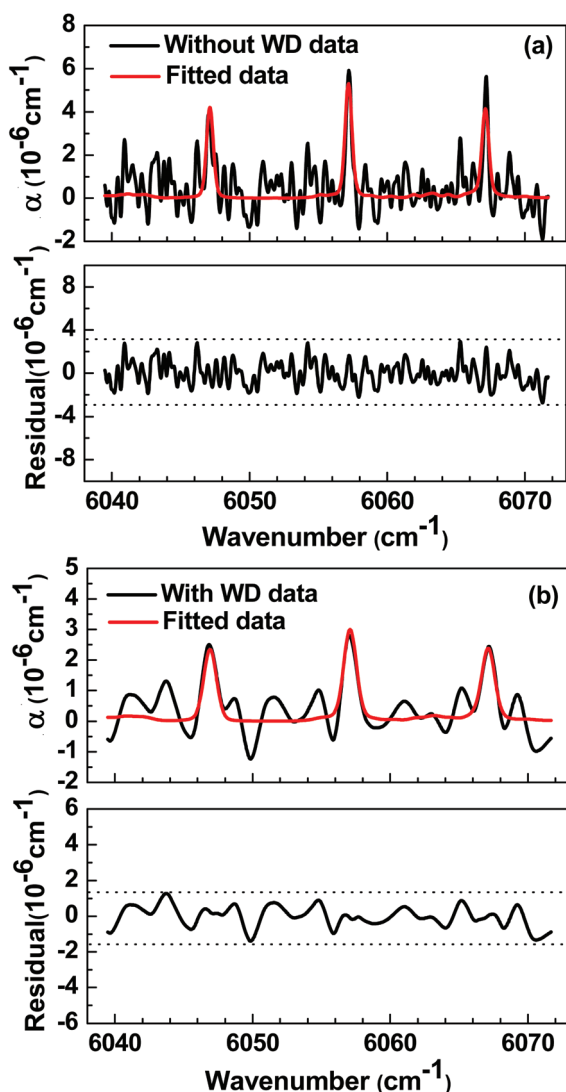

Fig. 11 (a) Experimental absorption spectrum of CH_4 measured by FT-IBBCEAS without WD processing (black lines) as well as the fitted spectral data (red line). Residual spectrum shown below indicates a standard deviation of 8.5×10^{-7} cm^{-1}. (b) Absorption spectra with WD processing to improve the detection precision (black line) and the fitted spectrum (red line). The standard deviation of the residual spectrum is improved to 4.6×10^{-7} cm^{-1}.

Conflicts of interest

There are no conflicts to declare.

Acknowledgements

Notes and references

1 C. Amiot, A. Aalto, P. Ryczkowski, J. Toivonen and G. Genty, *Appl. Phys. Lett.*, 2017, **111**, 061103.

2 S. S. Kiwanuka, T. K. Laurila, J. H. Frank, A. Esposito, K. Blomberg von der Geest, L. Pancheri, D. Stoppa and C. F. Kaminski, *Anal. Chem.*, 2012, **84**, 5489–5493.

3 J. J. Scherer, J. B. Paul, J. Hong and A. O'Keefe, *Appl. Opt.*, 2001, **40**, 6725–6732.

4 S. M. Ball, I. M. Povey, E. G. Norton and R. L. Jones, *Chem. Phys. Lett.*, 2001, **342**, 113–120.

5 S. M. Ball and R. L. Jones, *Chem. Rev.*, 2003, **103**, 5239–5262.

6 M. J. Thorpe, K. D. Moll, R. J. Jones, B. Safdi and J. Ye, *Science*, 2006, **311**, 1595–1599.

7 M. J. Thorpe, D. D. Hudson, K. D. Moll, J. Lasri and J. Ye, *Opt. Lett.*, 2007, **32**, 307–309.

8 T. Gherman and D. Romanini, *Opt. Express*, 2002, **10**, 1033–1042.

9 M. J. Thorpe, D. Balslev-Clausen, M. S. Kirchner and J. Ye, *Opt. Express*, 2008, **16**, 2387–2397.

10 T. Gherman, E. Eslami, D. Romanini, S. Kassi, J. C. Vial and N. Sadeghi, *J. Phys. D: Appl. Phys.*, 2004, **37**, 2408–2415.

11 S. E. Fiedler, A. Hese and A. A. Ruth, *Chem. Phys. Lett.*, 2003, **382**, 447–453.

12 J. M. Langridge, S. M. Ball and R. L. Jones, *Analyst*, 2006, **131**, 916–922.

13 T. Gherman, D. S. Venables, S. Vaughan, J. Orphal and A. A. Ruth, *Environ. Sci. Technol.*, 2008, **42**, 890–895.

14 T. Wu, W. Chen, E. Fertein, F. Cazier, D. Dewaele and X. Gao, *Appl. Phys. B*, 2012, **106**, 501–509.

15 B. Fang, W. Zhao, X. Xu, J. Zhou, X. Ma, S. Wang, W. Zhang, D. S. Venables and W. Chen, *Opt. Express*, 2017, **25**, 26910–26922.

16 H. Wang, J. Chen and K. Lu, *Atmos. Meas. Tech.*, 2017, **10**, 1465–1479.

17 R. S. Watt, T. Laurila, C. F. Kaminski and J. Hult, *Appl. Spectrosc.*, 2009, **63**, 1389–1395.

18 W. Denzer, M. L. Hamilton, G. Hancock, M. Islam, C. E. Langley, R. Peverall and G. A. D. Ritchie, *Analyst*, 2009, **134**, 2220–2223.

19 W. Denzer, G. Hancock, M. Islam, C. E. Langley, R. Peverall, G. A. D. Ritchie and D. Taylor, *Analyst*, 2011, **136**, 801–806.

20 A. Aalto, G. Genty, T. Laurila and J. Toivonen, *Opt. Express*, 2015, **23**, 25225–25234.

21 S. Chandran and R. Varma, *Spectrochim. Acta, Part A*, 2015, **153**, 704–708.

22 D. M. O'Leary, A. A. Ruth, S. Dixneuf, J. Orphal and R. Varma, *J. Quant. Spectrosc. Radiat. Transfer*, 2012, **113**, 1138–1147.

23 J. Orphal and A. A. Ruth, *Opt. Express*, 2008, **16**, 19232–19243.

24 A. A. Ruth, J. Orphal and S. E. Fiedler, *Appl. Opt.*, 2007, **46**, 3611–3616.

25 C. I. Salis, A. E. Malissovas, P. A. Bizopoulos and A. T. Tzallas, *IEEE, Int. Conf. Bioinform. Bioeng.*, 2013, **7789**, 1–4.

26 J. Li, B. Yu, W. Zhao and W. Chen, *Appl. Spectrosc. Rev.*, 2014, **49**, 666–691.

27 T. Wu, W. Chen, E. Kerstel, E. Fertein, X. Gao, J. Koeth, K. Rößner and D. Bruekner, *Opt. Lett.*, 2010, **35**, 634–636.

28 F. Ehrentreich, *Anal. Bioanal. Chem.*, 2002, **372**, 115–121.

29 X. Lu, H. Liu, J. Kang and J. Cheng, *Anal. Chim. Acta*, 2003, **484**, 201–210.

30 M. Niu, P. Han, L. Song, D. Hao, J. Zhang and L. Ma, *Opt. Express*, 2017, **25**, 896–905.

31 T. Wu, W. Zhao, W. Chen, W. Zhang and X. Gao, *Appl. Phys. B*, 2009, **94**, 85–94.